

Possible orthopyroxene enrichment in the upper mantle below the Mississippi Embayment

Arushi Saxena¹, Eunseo Choi¹, Christine A. Powell¹, Charles A. Langston¹

¹Center for Earthquake Research and Information, The University of Memphis

Key Points:

- Possible origins of similar-magnitude and negative (-5 to 6%) V_p and V_s anomalies at depths 100 to 250 km beneath the NMSZ are explored
- A combination of elevated temperature and water content cannot explain V_p and V_s anomalies
- The V_p and V_s anomalies can be explained by an orthopyroxene content of upto 40% along with temperature variations

arXiv:1810.11159v1 [physics.geo-ph] 26 Oct 2018

Corresponding author: Arushi Saxena, asaxena@memphis.edu

Abstract

A high-resolution tomography study for the mantle beneath the New Madrid Seismic Zone (NMSZ), a major intraplate earthquake zone in the Central and Eastern US, reveals 3 - 5 % low Vp and Vs anomalies in the upper mantle in the depth range 100 to 250 km. When attributed only to temperature variations, such low velocities lead to temperatures higher than the olivine solidus, for which consistent observational support is lacking. Similar magnitudes of the Vp and Vs anomalies also suggest that temperature anomalies are unlikely to be the sole factor because Vs is more sensitive to temperature than Vp. In this study, we attribute the velocity anomalies to elevated water and orthopyroxene (Opx) contents as well as temperature variations. We then compute differential stresses using three-dimensional numerical models subjected to a loading similar to the regional stresses. The models assume a Maxwell viscoelastic crust and mantle with viscosities based on the temperature, water and Opx content converted from the tomography. We find that the presence of water allows for sub-solidus variations in temperature. However, any combination of water content and temperature anomalies fails to yield Vp and Vs anomalies of a similar magnitude. Thus, we consider Opx enrichment in place of water content. Our calculations show that reasonable Opx content and sub-solidus temperatures can explain both Vp and Vs anomalies. We speculate that the Opx enrichment could have been produced by fluids released from a stagnant piece of the Farallon slab imaged at around 670 km beneath the NMSZ.

1 Introduction

The New Madrid Seismic Zone (NMSZ), located in the Northern Mississippi Embayment, is a seismically active region as indicated by paleoseismic evidence (e.g., Tuttle, 2002) and three historic large ($M_w > 7$) earthquakes in 1811- 1812 (Bakun & Hopper, 2004; Johnston, 1996). Numerous small-magnitude earthquakes ($M_w < 5$) are still being recorded (Fig. 1) posing a potential risk of seismic hazard in and around this zone.

Geodetic strain rates observed in this region are less than 3×10^{-9} /yr (Boyd, Smalley, & Zeng, 2015). This value is much lower than the strain rate loading of active plate boundaries suggesting that the earthquake generation is not entirely associated with plate tectonics. This has puzzled researchers, invoking them to come up with alternative mechanisms to explain the seismicity of NMSZ that are compatible with the field observations.

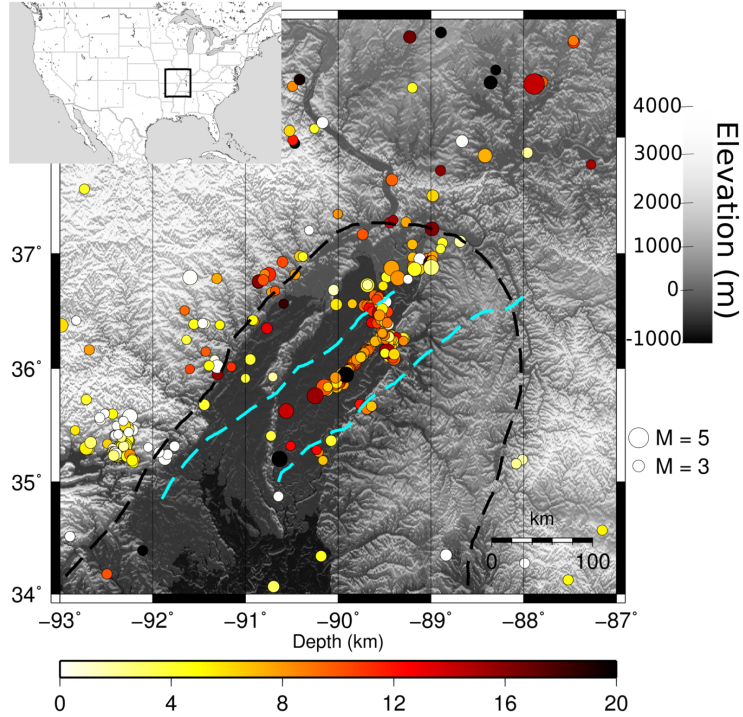


Figure 1. Earthquake epicenters ($>M_w2.0$) in the New Madrid Seismic Zone (NMSZ) from May, 2002 to May, 2017. The color and size of symbols represent the depth and magnitude, respectively. The black line marks the boundary of the Mississippi Embayment and the Reelfoot Rift is contained within the blue dashed line. The inset shows a part of the North American and the U.S. state borders providing a geographic reference for the location of the NMSZ (black square). The earthquake catalogue is obtained from the United States Geological Survey at <https://earthquake.usgs.gov/earthquakes/search/>. This figure is available under CC-BY ?.

The existing models for the NMSZ seismicity cannot explain all of the existing seismic and other geophysical observations, calling for an improved model. Previous studies that proposed lower lithospheric strength (Liu & Zoback, 1997), weaker lower crust (Kenner, 2000), deglaciation of the Laurentide ice sheet (Grollimund & Zoback, 2001), sinking of a denser heterogeneous lower crust (Pollitz, 2001), and higher mantle temperatures (Zhan, Hou, Kusky, & Gregg, 2016) in the NMSZ than in the surrounding region would elevate the stress level and therefore promote seismicity. However, although required to be weak by some models (Kenner, 2000; Liu & Zoback, 1997), the lower crust in the NMSZ is strong due to the presence of a dense mafic intrusion (commonly called a pillow) (Mooney, Andrews, Ginzburg, Peters, & Hamilton, 1983; Rabak, Langston, &

Powell, 2011) possibly created by the passage of the Bermuda hotspot during mid-Cretaceous (Chu, Leng, Helmberger, & Gurnis, 2013; R. Cox & Arsdale, 1997; R. T. Cox & Arsdale, 2002). Attributing the seismic speed variations in the region's upper mantle only to anomalous temperature (Zhan et al., 2016) also seems inconsistent with more recent high resolution tomographic observations (Chen et al., 2016; Chen, Zhao, & Wu, 2014; Nyamwandha, Powell, & Langston, 2016). Chen et al. (2014) and Chen et al. (2016) found 5 % V_p and 7 % V_s decrease at depths of 75-150 km beneath the NMSZ, respectively. When converted to temperature variations only, seismic velocity anomalies of this magnitude would mean partial melting in the upper mantle. This is not supported by surface heatflow observations. Since V_s is more sensitive to temperature (e.g., Cammarano, Goes, Vacher, & Giardini, 2003; Goes, Govers, & Vacher, 2000) and the presence of melt alters V_s more than V_p (Karato, 2003), V_s and V_p anomalies of a similar magnitude (3% -5%) observed by Nyamwandha et al. (2016) cannot be explained by temperature variations alone.

We note that two recent regional tomographic studies in the Central and Eastern United States (CEUS) (Chen et al., 2016; Nyamwandha et al., 2016) independently attributed their observed low velocity anomalies not only to elevated temperature but also to other factors such as the presence of water and compositional variations. The presence of orthopyroxene (Opx) lowers V_p more than V_s (Schutt & Leshner, 2010) and provides a possible explanation for the similar magnitudes of the V_p and V_s anomalies in the presence of elevated temperature. Previous studies have reported Opx enrichment over flat subducted slabs (e.g., Tang et al., 2012; Wagner, Anderson, Jackson, Beck, & Zandt, 2008).

We propose that Opx enrichment occurs from the flat Laramide slab below the NMSZ (Sigloch, McQuarrie, and Nolet 2008) at mantle transition depths, altering the composition and hydrating the above lying lithosphere. Similar reasoning is invoked to explain the tomographic and geochemical observations in the North China Craton (NCC) (e.g., Santosh, Zhao, & Kusky, 2010; Q. Wang, Bagdassarov, Xia, & Zhu, 2014; Zhang, Zheng, & Zhao, 2009) in which asthenospheric upwellings from the stagnant Pacific slab altered the lithosphere.

To address this idea in our study, we constrain the upper mantle viscosity beneath the NMSZ assuming that the low velocity anomalies found in the Nyamwandha et al. (2016) tomography results come from temperature, water and Opx. We compute differ-

ential stresses at seismogenic depths using the viscosity distributions as an input for geodynamic numerical models and include the effects of compositional variations accounting for possible enrichment in Opx.

2 Modeling Methods

2.1 Viscosity Calculations

2.1.1 Case I: Temperature only

Effective viscosity for power law creep is given as (Kirby & Kronenberg, 1987):

$$\eta_{eff} = \dot{\epsilon}^{\frac{1-n}{n}} A^{-1/n} \exp\left(-\frac{H}{nRT}\right), \quad (1)$$

where $\dot{\epsilon}$ is the effective strain rate taken as $3.25 \times 10^{-17} \text{ s}^{-1}$ for our calculations Calais, Han, DeMets, and Nocquet (2006), R is the gas constant, A is the pre-exponential factor, n is the power law exponent, H is the activation energy and T is the temperature. The values of A , n and H as well as density for each layer are listed in Table 1. .

Table 1. Rheological constants used in our model simulations

Layer	Composition	Density (kg/m ³)	A (MPa ⁻ⁿ s ⁻¹)	n	H (kJ mol ⁻¹)
Upper crust ^a	Quartzite	2750	$1.1 e^{-4}$	4.0	223
Lower crust ^a	Granulite	2900	$1.4 e^4$	4.2	445
Mantle ^b	Olivine	3200	$1.1 e^5$	3.5	530

a : Burov (2010), *b* : Dixon, Dixon, Bell, and Malservisi (2004)

We calculate temperature anomalies using the Vp and Vs anomalies, denoted as ∂Vp and ∂Vs hereafter, determined by Nyamwandha et al. (2016). The sensitivities of Vp and Vs to temperature are based on the anelastic and anharmonic effects in olivine (Ol) and are originally given in Goes et al. (2000) as follows:

$$\begin{aligned} \frac{\partial Vp}{\partial T} &= \frac{1}{2Vp_0 \rho} \frac{\partial K}{\partial T} + \frac{2}{3Vp_0 \rho} \frac{\partial \mu}{\partial T} + Q_p^{-1} \frac{aH}{2RT_0^2 \tan(\pi a/2)}, \\ Q_p &= A\omega^a \exp\left[\frac{a(H + PV)}{RT_0}\right] \frac{3Vp_0^2}{4Vs_0^2}, \\ \frac{\partial Vs}{\partial T} &= \frac{1}{2Vs_0 \rho} \frac{\partial \mu}{\partial T} + Q_s^{-1} \frac{aH}{2RT_0^2 \tan(\pi a/2)}, \\ Q_s &= A\omega^a \exp\left[\frac{a(H + PV)}{RT_0}\right]. \end{aligned}$$

Density is assumed to be constant as its sensitivity to temperature is about 4 orders of magnitude smaller than those of the elastic moduli when the standard value of volume expansion coefficient ($10^{-5}/\text{K}$) is assumed. Table 2 lists the values of parameters and relevant quantities. The reference velocities (V_{p_0} , V_{s_0}) and the reference temperature (T_0) are depth-dependent (Fig. 2). We use the velocity model from Pujol, Johnston, Chiu, and Yang (1997) for the crustal depths (< 40 km) and IASP91 (Kennett & Engdahl, 1991) for the mantle (> 40 km). The reference temperatures are taken from Table 2 in Zhan et al. (2016), which are originally from Liu and Zoback (1997) for depths shallower than 100 km and from Goes and van der Lee (2002) for greater depths.

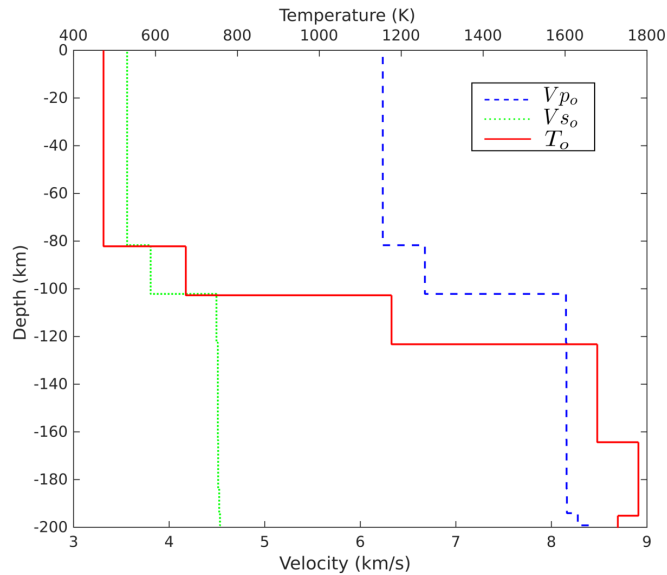


Figure 2. Reference P and S wave velocities (V_{p_0} and V_{s_0}) used by Nyamwandha et al. (2016) for their tomography results and reference temperature (T_0) from Liu and Zoback (1997) and Goes and van der Lee (2002) based on which the temperature anomalies are calculated. This figure is available under CC-BY ?.

2.1.2 Case II: Temperature and water

Velocity anomalies are assumed to be a function of water content as well as temperature in this case. For simplicity, we assume uniform distributions of water that are completely independent of velocity and temperature variations. The effective viscosity is derived from the power law creep under the constant strain rate assumption (Dixon

Table 2. Elastic moduli, their temperature derivatives and anelasticity parameters

Variable	Symbol	Unit	Value
Bulk modulus ^a	K	GPa	129
Shear modulus ^a	μ	GPa	82
Derivative with temperature ^a	$\partial K/\partial T$	MPa/K	-16
	$\partial\mu/\partial T$	MPa/K	-14
Angular frequency ^b	ω	rad/s	2π
Frequency exponent ^{a,c}	a	N/A	0.15
Gas constant	R	J/mol·K	8.314
Activation energy ^{a,c}	H	kJ/mol	500
Volume ^{a,c}	V	cm ³ /mol	20

a: Goes et al. (2000), *b*: based on the frequency range of the tomography by Nyamwandha et al. (2016), *c*: Sobolev et al. (1996).

et al., 2004):

$$\eta_{eff} = \dot{\epsilon}^{\frac{1-n}{n}} C_{OH}^{-\frac{r}{n}} A^{-\frac{1}{n}} \exp\left(-\frac{H}{nRT}\right). \quad (2)$$

where r is the fugacity exponent, assumed to be 1.2 (Hirth & Kohlstedt, 2003), C_{OH} is water content in Ol given in the unit of H/10⁶ Si. Under the current assumption, the temperature T for (2) is the reference temperature, T_0 from Fig. 2. Parameters for the upper and lower crust are listed in Table 1 and those for the mantle are taken from Hirth and Kohlstedt (2003).

We consider two possible scenarios for water concentration in olivine following Dixon et al. (2004): Damp (50 ppm H₂O) and wet (fully saturated with water). Although it is not realistic to assume that the water distributions are uniform throughout our model domain, we explore these scenarios to assess the viscosity-lowering effects of the water content.

2.1.3 Case III: Temperature and water added selectively

We assume that mantle temperatures are likely to be lower than the olivine solidus (T_m) everywhere in the study area. This is because the presence of melt would alter V_s more than V_p (Karato, 2003) but the region's tomography results show similar magni-

tudes of ∂V_p and ∂V_s . If computed as in Case I, temperatures (T_I) would exceed T_m at some locations (Fig. 3). Only at those locations, we attribute the excess temperature ($T_{ex} = T_I - T_m$) to the presence of water such that $\partial V_p = \partial V_p^{T_m} + \partial V_p^{OH}$, where $\partial V_p^{T_m}$ is the Vp anomaly due to $T_m - T_0$ and ∂V_p^{OH} is contribution to the Vp anomaly from the water. We use the following relationship between fluid content and velocity anomaly (Karato & Jung, 1998):

$$\delta C_{OH} = -\frac{\partial V^{OH}}{V_o(T, P)} \left(2 \tan \frac{\pi \alpha}{2} \right) \frac{\omega}{\alpha B} \left(\frac{A}{\omega} \right)^{1-\alpha} \exp \left(\alpha \beta \frac{T_m}{T_0} \right), \quad (3)$$

where ∂V^{OH} is $\partial V_p - \partial V_p^{T_m} = \partial V_p - \partial V_p / \partial T (T_m - T_0)$, T_m is the Ol solidus and T_0 is the reference temperature. $V_o(T, P)$ is the reference velocity, $\omega = 2\pi$ rad/s (Table 2), β is related to enthalpy H (in Table 1) as $H = \beta R T_m$ (Karato & Jung, 1998), $A = B = 8.8 \times 10^6$ and $\alpha = 0.3$, which corresponds to the half space cooling model from Karato and Jung (1998). δC_{OH} is calculated in ppm H/Si assuming that the reference state has no water content i.e. $C_{OH} = 0$.

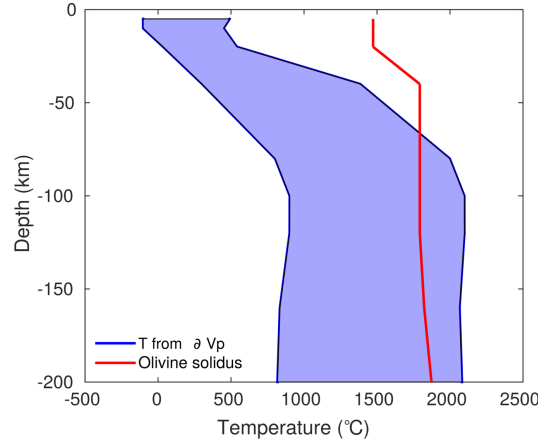


Figure 3. Minimum and maximum temperatures (blue lines) calculated from P wave anomalies as in Case I; and the solidus (red line) from Herzberg (1983). This figure is available under CC-BY ?.

2.1.4 Case IV: Temperature and Opx

Opx enrichment, together with temperature variations, may explain the ∂V_p and ∂V_s of similar magnitudes because Vp is known to be more sensitive to Opx concentration than Vs (Schutt & Lesher, 2010) while Vs is more sensitive to temperature than Vp.

We therefore consider the combined effects of Opx and temperature on Vp and Vs anomalies as follows:

$$\partial V_k = \frac{\partial V_k}{\partial T} \delta T(X_{Opx}) + \frac{\partial V_k}{\partial X_{Opx}} \delta X_{Opx}, \quad (4)$$

where V_k denotes Vs or Vp, X_{Opx} is the Opx volume fraction in vol % and T is temperature (K). The coefficients are defined by the Voigt scheme: i.e. in case of Vs,

$$\frac{\partial V_s}{\partial T} = \frac{\partial V_s}{\partial \mu} \frac{\partial \mu}{\partial T} = \frac{1}{2V_s \rho} \frac{\partial}{\partial T} [(1 - X_{Opx}) \mu_{Ol} + X_{Opx} \mu_{Opx}],$$

where ρ is the reference density, μ , μ_{Ol} and μ_{Opx} are shear moduli for the bulk composition, pure Ol and pure Opx, respectively. The sensitivities of elastic moduli to temperature for Ol and Opx are taken from Goes et al. (2000) and the sensitivities of Vp and Vs to Opx content from Schutt and Lesher (2010). We invert the above equations for X_{Opx} and δT simultaneously using the Newton-Raphson scheme assuming that Opx concentration is zero in the reference state.

There is no wide consensus on whether the presence of Opx would generally strengthen or weaken the mantle (e.g., Hansen & Warren, 2015; Ji, Wang, & Wirth, 2001; McDonnell, Peach, van Roermund, & Spiers, 2000; Sundberg & Cooper, 2008; Tasaka, Hiraga, & Zimmerman, 2013; Tikoff, Larson, Newman, & Little, 2010)). We calculate bulk viscosity in the presence of Opx using a constant strain scheme as $\eta = (1 - X_{Opx})\eta_{ol} + X_{Opx}\eta_{opx}$ (e.g., Ji et al., 2001). In one model, we assume that Opx viscosity is 3.3 times that of Ol (Hansen & Warren, 2015) for strengthening effects and in another we construct a model in which Opx viscosity is one eighth of Ol viscosity (Ji et al., 2001) to account for weakening effects of Opx.

2.2 Differential Stress Calculations

We construct three-dimensional (3D) models with Maxwell linear viscoelastic rheology to compute differential stresses. Each model has three layers: upper crust (0-20 km), lower crust (20-40 km,) and mantle (40-200 km) (Fig. 4a). The lateral extent of our model is 2665×2554 km. The central region (gray box) is constrained by the Nyamwandha et al. (2016) tomography results (Fig. 4a) but the overall domain is set to be much greater than that of the tomography in order to reduce boundary effects.

To simulate northeast-trending regional compressional principal stress (σ_1) (M. L. Zoback & Zoback, 1989), horizontal velocities with a magnitude of 10 cm/yr are applied on the

X- and Y-axis-perpendicular faces (Fig. 4b) until the differential stress ($|\sigma_1 - \sigma_3|$) of 200 MPa is achieved at the depth of 10 km (Baird, McKinnon, & Godin, 2010; M. D. Zoback et al., 1993). After that, the boundary velocity magnitude is reduced to avoid further increasing the differential stress but is set to a non-zero value, 0.1 cm/yr, to maintain this stress state without complete viscous relaxation. The top surface is free (i.e., zero-traction) and the bottom has a no-slip condition.

We discretize the domain into a mesh with 227448 hexahedral tri-linear elements using Trellis 15.0. The mesh has lateral and vertical resolutions of 25 and 5 km, respectively. We use Pylith (Aagaard, Knepley, & Williams, 2013), an open source finite element code for crustal dynamics developed and distributed by Computational Infrastructure for Geodynamics, to calculate stresses and displacements under the loading conditions described above. Differential stresses are derived from stress solutions at one location in the NMSZ marked by the purple line in Fig. 4a.

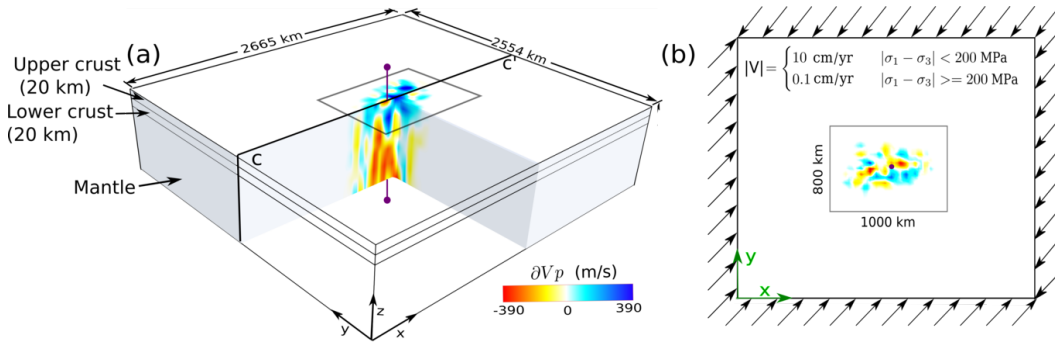


Figure 4. (a) Model domain and the P wave anomalies from Nyamwandha et al. (2016). The domain has 3 layers: 20 km-thick upper crust, 20 km-thick lower crust and mantle. The purple vertical line through the NMSZ marks the location of vertical profiles of model results shown in the subsequent figures. The rectangle on the surface represent the spatial extent of the tomography model. (b) Cross-section of the model domain and S wave anomalies from Nyamwandha et al. (2016) at 100 km depth. Arrows denote the velocity boundary conditions applied on the side walls. This figure is available under CC-BY ?.

2.3 Caveats regarding model setup

We assume that the reference state for the tomography has uniformly zero Opx concentration. When a non-zero initial Opx concentration is assumed, the Opx change calculated from inversion is reduced by the initial amount assumed, keeping the total Opx concentration the same. The inverted temperatures are also reduced by 20 K if we assume an initial Opx concentration of 20 %, although we do not show the results with different initial opx concentration.

Also, although the magnitude of the temperature anomaly is reduced when water is present, the temperature due to our maximum calculated water content in Case III (~ 40 ppm H/Si) changes by ~ 1 % from the original value (Karato, 2003), which we neglect in our calculations. We explore Case II only to observe the weakening effects on viscosity due to the presence of water, therefore, it is acceptable to consider temperature independently from water content.

Our model setup does not include the effects of gravity and it is assumed that the density of all 3 layers, upper crust, lower crust, and mantle, is constant within each layer. Since we are interested only in the effects of local mantle heterogeneity on the overlying crust, gravity in our model setup can be neglected. Additionally, ignoring density contrasts due to temperature anomalies is justifiable as the volumetric expansion coefficient for common rocks is $\sim 10^{-5}/\text{K}$ and for maximum temperatures calculated here, 600 K, this amounts to 0.6% change in the density. We also ignore the effects of density on composition in Eq. 6 and take the bulk density as 3220 kg/m³ using the average of the densities of Ol (3222 kg/m³) and Opx (3218 kg/m³). This assumption is reasonable as the densities of Ol and Opx (taken from Goes et al. (2000)) are similar and using average density introduces a maximum change of 0.06 % compared to the case where density is calculated by the weighted average.

We also assess the effects of the Reelfoot Rift (Fig. 1) by imposing -6 % Vp and Vs anomalies in the rift (Pollitz & Mooney, 2014) modeled as ~ 70 km wide on the surface, narrowing to ~ 35 km at the depth of 10 km (Marshak & Paulsen, 1996). With the imposed low velocity anomalies, viscosities within the rift are lower than the surrounding areas and therefore, the resultant differential stresses from the model with the rift are lower than the models without rifts. This observation is consistent with the effects of rift zones found by Zhan et al. (2016). We do not show the model results with the rift

as we are interested in explaining the cause of the low-velocity anomaly (>50 km depths) and its impact on the NMSZ seismicity. The presence of rifts lowers the absolute differential stress in the upper crust by ~ 10 MPa but does not change the relative impact on differential stress among the cases investigated in this study.

3 Model Results

3.1 Case 1: Temperature only

We convert ∂V_p and ∂V_s to temperature variations using (2) and (2). Temperature anomalies are plotted in Fig. 5 at different depths with best-fitting linear trends (black solid lines, Fig. 5). If both ∂V_p and ∂V_s are simultaneously explained by temperature only, the converted temperatures should be equal falling on a line with the slope equal to 1 (red lines, Fig. 5) and the magnitudes of ∂V_s would be greater than those of ∂V_p because V_s has greater sensitivity to temperature than V_p . However, slopes of the best-fitting lines are in the range 0.5 to 0.7 at all depths, consistently smaller than one because ∂V_p and ∂V_s have similar magnitudes in the tomography by Nyamwandha et al. (2016).

We show one of the viscosity calculations based on the ∂V_p -converted temperature anomalies at cross-section C-C' (see Fig. 4) in Fig. 6. The V_p anomalies from Nyamwandha et al. (2016) along this cross-section are shown in Fig. 6a. According to the V_p sensitivity to temperature, (2), and parameters in Table 2, the temperature variations are in the range ± 600 K (Fig. 6b). We compute the viscosity using (1) and the total temperature, which is the sum of the reference geotherm (Fig. 2) and the temperature variations. The viscosity distribution (Fig. 6c) follows the pattern of velocity and temperature variations and the minimum is about 10^{20} Pa·s where V_p is the smallest.

3.2 Case II: Temperature and uniform water content

We compute differential stresses within the NMSZ based on the reference temperature (Fig. 2) and a spatially-uniform concentration of H_2O in olivine: 50 ppm (damp) and water saturated concentration (wet) (Fig. 7a). We compare our calculations with the viscosity computed from ∂V_p -converted temperatures as in Case I and no water content, referred as the dry case ($C_{OH} = 0$ ppm) subsequently. Given the same temperature, water can reduce differential stress in the upper mantle (depths ≥ 40 km) by or-

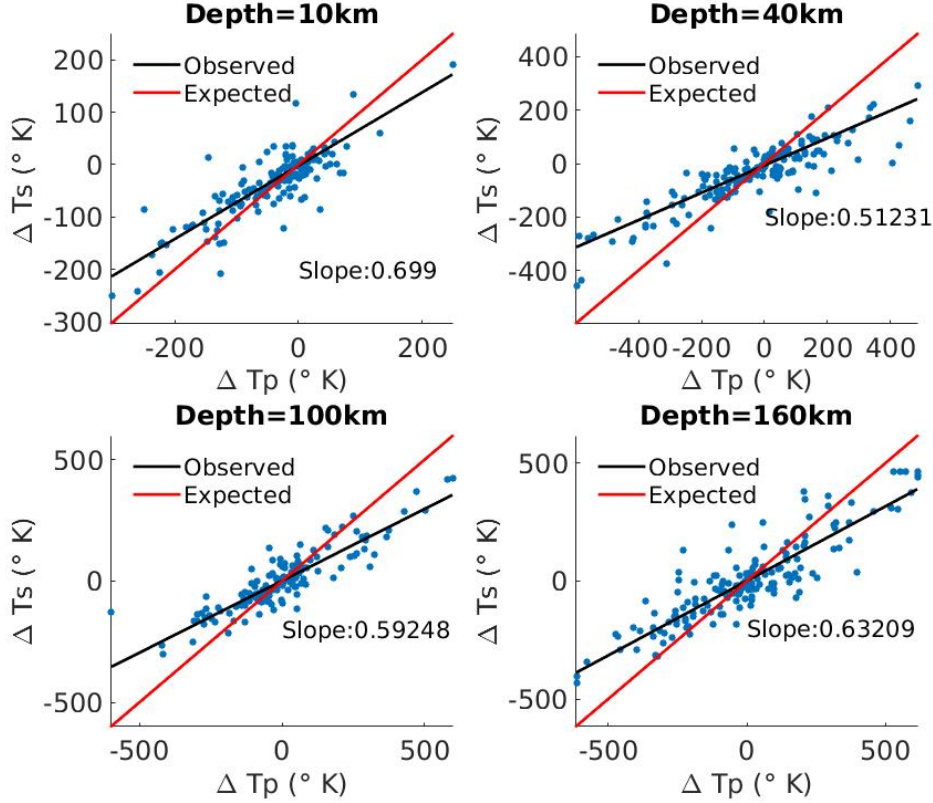


Figure 5. Scatter plots of temperature anomalies calculated from P wave (ΔT_p) and S wave (ΔT_s) anomalies with the best-fitting lines (black). The red line has a slope equal to 1, representing the case where both V_p and V_s anomalies are due to temperature only. This figure is available under CC-BY ?.

orders of magnitude but in the upper crust, differential stress increases with water content by about 2 MPa (Fig. 7b). The same effect of water content on differential stress level in the upper crust is seen in the models based on V_s anomalies (not shown here).

3.3 Case III: Temperature and selectively-added water

We compute water content in the super-solidus regions identified in Case I (Fig. 3) using (3) and plot the contours of the calculated water contents on the V_p anomalies calculated from the temperatures in the super-solidus region, ∂V_p^{ex} , at a depth 150 km and in the cross section (marked in Fig. 4) in Fig. 8. The correlation between the

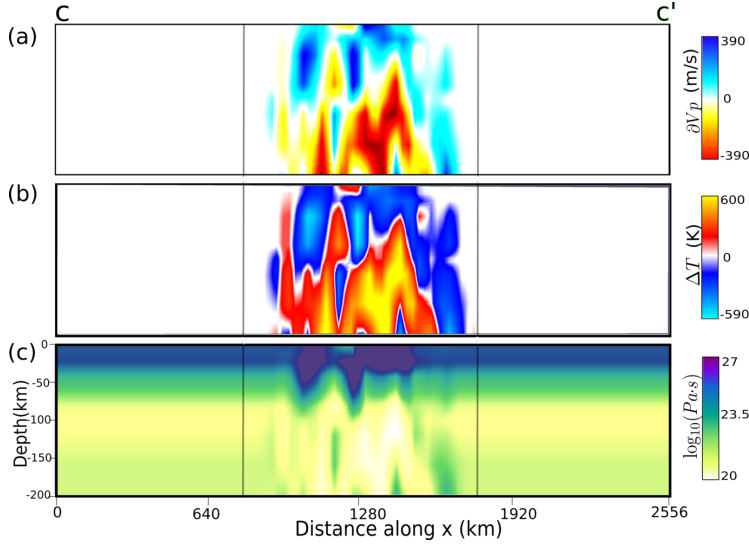


Figure 6. Conversion of the velocity anomalies into model viscosities at cross-section CC' in Fig. 4a. Thin vertical gray lines mark the boundaries of the tomography domain of Nyamwandha et al. (2016) (see Fig. 4a). Vertical axis is exaggerated by a factor of 3. (a) P-wave velocity anomalies (∂V_p) from Nyamwandha et al. (2016). (b) Temperature anomalies calculated based on ∂V_p . (c) Viscosities computed based on the temperatures anomalies in (b) and the reference temperature shown in Fig. 2. This figure is available under CC-BY ?.

calculated water content and low ∂V_p is clearly seen in the cross section and the depth section (Fig. 8). For our calculations from the velocity anomalies (3), water contents reach up to 50 ppm in low- V_p regions.

Based on the water content only in the supersolidus regions, we calculate the viscosity distribution using (2) and the parameters in Table 1 within the NMSZ (Fig. 4). The resultant differential stresses in the NMSZ upper crust are compared with the dry model (Case I) in Fig. 9b. A minor decrease in viscosity due to the weakening effect of the water is seen only in the depth range from 120 to 160 km, where significant water content is calculated (Fig. 9a). Differential stresses also show only minor differences between the dry model and the present model over the same depth range (Fig. 9b).

3.4 Case IV: Temperature and Opx content

We compute Opx volume fraction (X_{Opx}) and temperature anomalies (ΔT) that simultaneously satisfy ∂V_s and ∂V_p by solving the system of equations (4). Two depth

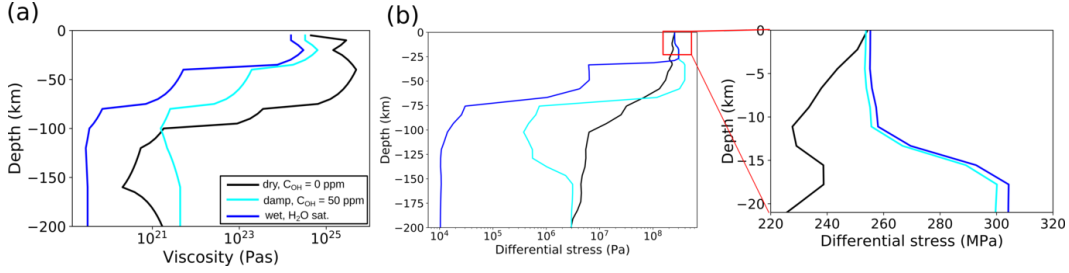


Figure 7. Depth profiles of (a) viscosity (b) differential stresses within the NMSZ (purple line in Fig. 4) for the model computed from Vp-based temperatures calculated in Case I (black), reference temperatures from Fig. 2 with uniform C_{OH} concentration of 50 ppm (cyan), reference temperatures from Fig. 2 with water-saturated olivine concentration (blue). Differential stresses (b) are zoomed into to observe the concentration in upper crust on the right. This figure is available under CC-BY ?.

slices at 100 and 160 km displaying X_{Opx} and ΔT are plotted in Fig.10. Since X_{Opx} is more sensitive to Vp and ΔT is more sensitive to Vs, we plot X_{Opx} and Vp together in the left panels and ΔT and Vs together in the right panels in Fig.10. X_{Opx} values show correlation with negative Vp anomalies, reaching a maximum of 0.2 at 100 km depth and 0.3 at 160 km. Temperature anomalies vary between ± 450 K. This magnitude of temperature anomalies is 10-20 % smaller than that of the dry, Opx-free case (Case I), which exhibited temperature anomalies of ± 600 and ± 500 K at the corresponding depths (Fig.6).

Differential stresses are computed under various assumptions on the effects of Opx enrichment on viscosity (Fig. 11). We consider three possibilities: Opx enrichment increases viscosity Hansen and Warren (2015), decreases it Ji et al. (2001), or has no effect on viscosity. Estimates for the sensitivity of viscosity to Opx contents are only loosely constrained (e.g., Hansen & Warren, 2015; Ji et al., 2001; McDonnell et al., 2000; Tasaka et al., 2013; Tikoff et al., 2010). Hansen and Warren (2015) suggest a factor of 1.2 to 3.3 increase in viscosity for a pyroxene fraction up to 30 %. Conversely, Ji et al. (2001) indicate a factor of 3 to 8 decrease in the strength of enstatite, the Mg end member of Opx, relative to fosterite, the Mg end member of Ol, for samples containing 0.4-0.6 volume fraction of fosterite. We choose a factor of 3.3 for increase and 8 for the decrease in Opx viscosity relative to Ol as end member cases. Our calculations for these three cases show

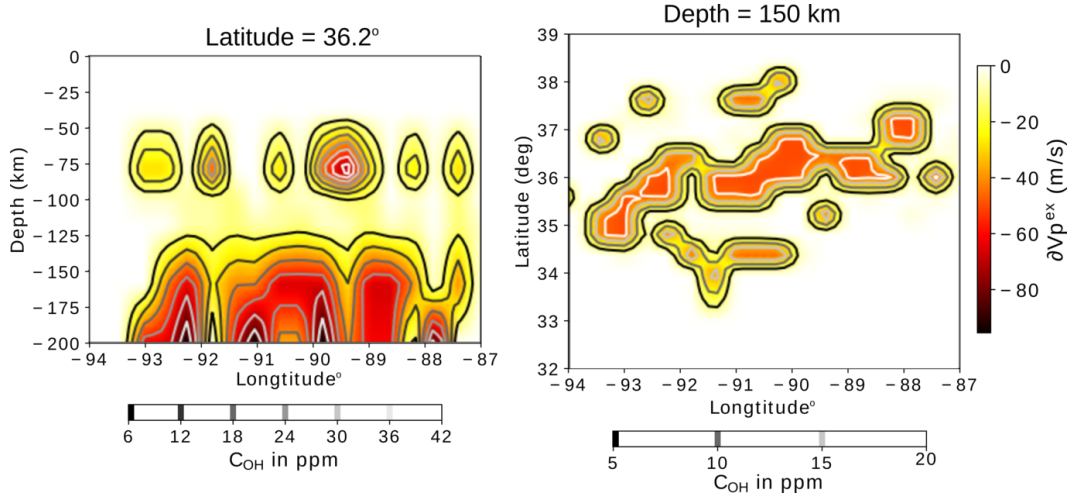


Figure 8. Selectively-added water contents based on the velocity anomalies converted from the temperatures in the super-solidus region shown on a cross-section along the latitude of 36.2° (left), which approximately coincides with CC' in Fig. 4 and on a depth section at 150 km (right). The lower velocities correspond to higher calculated water contents. This figure is available under CC-BY ?.

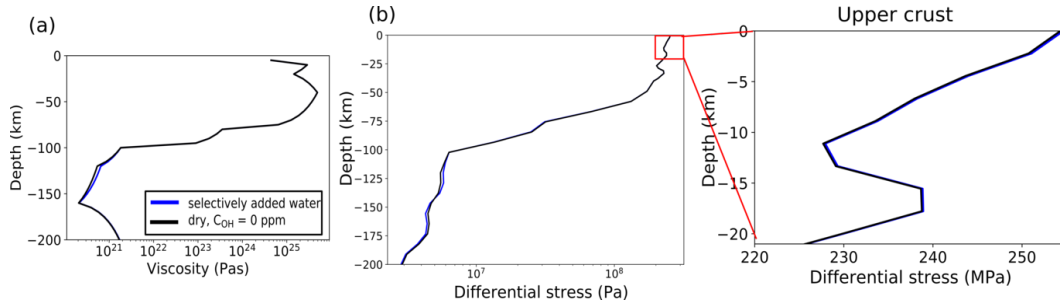


Figure 9. Same as Fig. 7 but for the model with selectively-added water in blue and the dry model described in Case I in black. This figure is available under CC-BY ?.

that the strengthening and weakening effects by Opx enrichment are insignificant (Fig. 11a). Differential stresses also show only about 1 % of variation at all depths (Fig. 11b).

4 Discussion

Differential stress calculated in all the cases described in the study is most sensitive to the temperature and less so to the Opx content and water content. Low differential stresses in the mantle in all the models (cases I-IV) are consistent with the high-temperature anomalies and low mantle viscosity values. Relatively strong crust (depths

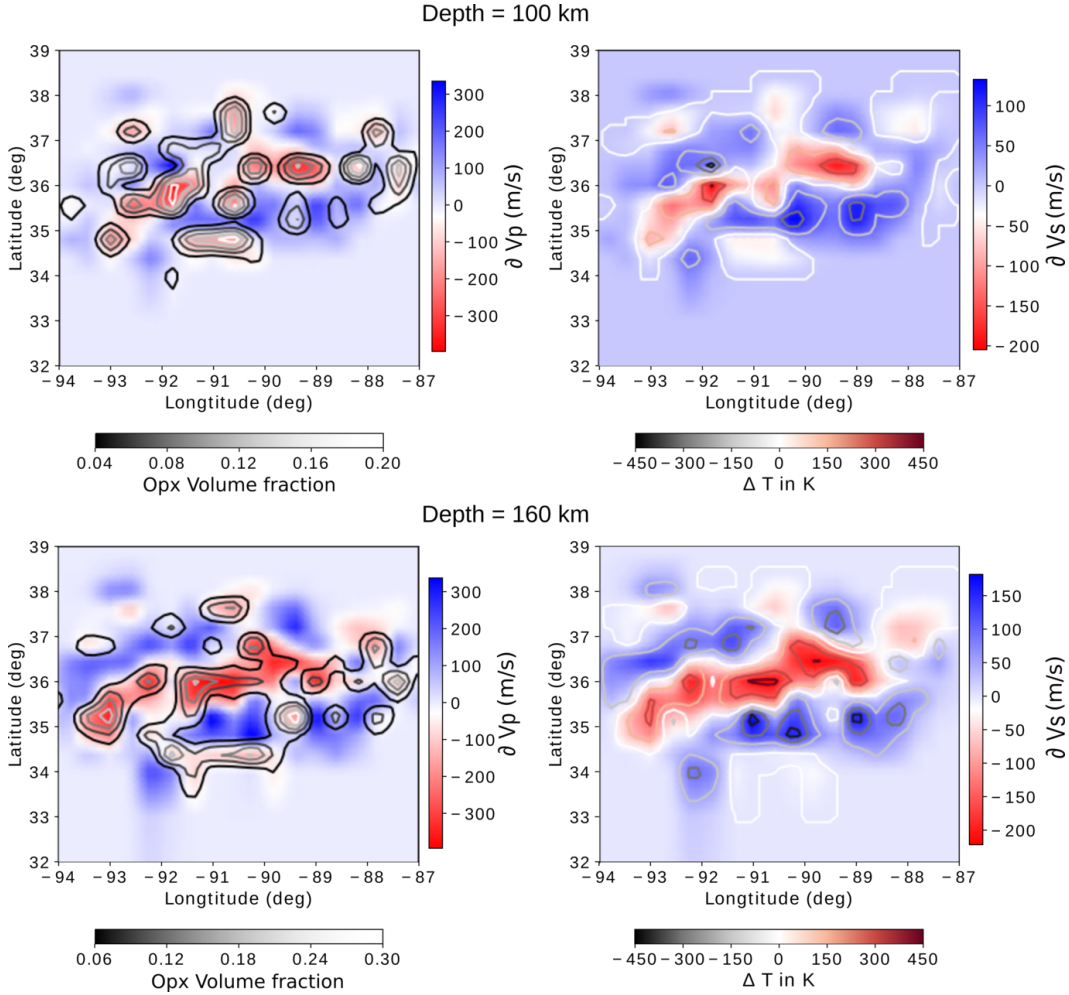


Figure 10. Inverted Opx contents and temperature anomalies at depths of 100 and 160 km. (left) V_p anomalies overlain by the contours of the Opx volume fraction. (right) V_s anomalies overlain by the contours of the temperature variations. This figure is available under CC-BY ?.

> 40 km) concentrates the differential stress from the deeper mantle. Differential stress in the upper crust calculated from the Opx-enriched cases (case IV) appears to be smaller than values computed using forward calculated temperatures (case I and II). This trend is the result of lower temperatures (Fig. 10) observed after inversion in case IV than the calculated temperatures in case I (Fig. 5), implying that the mantle in case I is weaker and concentrates higher differential stress in the upper crust (Fig. 12). It can also be observed from Fig. 12 that the effects of Opx on differential stress are minor. Capping the maximum temperatures computed from P wave anomalies (ΔT_p) with the olivine solidus and attributing the excess anomalies to water content (case III) has minor effect on the

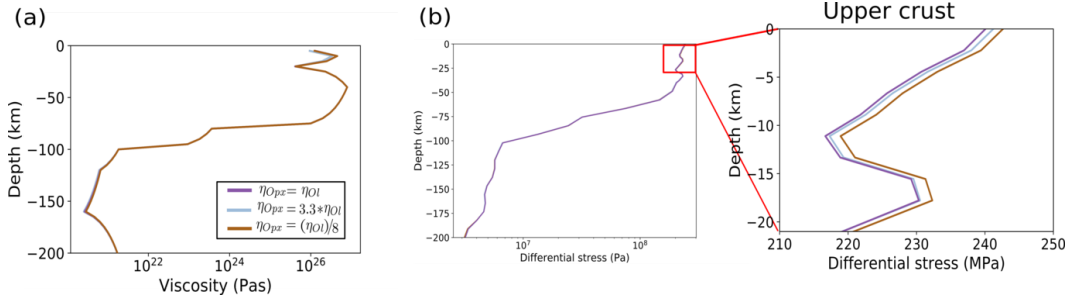


Figure 11. Same as Fig. 7 but for the models corresponding to the three possible effects of Opx enrichment on viscosity: Viscosity strengthening (light blue), viscosity weakening (brown) and the same viscosity as olivine (purple). This figure is available under CC-BY ?.

differential stress compared to case I. On the other hand, the differential stress calculated using uniform water content (case II) and the reference temperature (T_{ref}) differs appreciably from all the other cases (I, III) using the ∂V_p -calculated temperatures. Therefore it can be inferred from Fig.12 that the differential stress is most sensitive to the temperature.

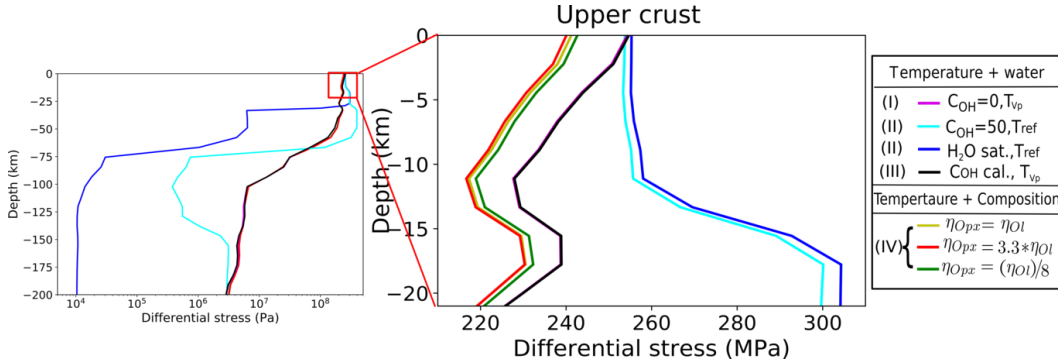


Figure 12. Depth profiles of differential stress from all the cases (Case I to IV) presented in this study. Case I: temperatures converted from the ∂V_p (purple); Case II: water added in the whole domain with the reference temperature (cyan and blue); Case III: selective addition of water in super-solidus region and temperature calculated from Case I using ∂V_p (black); Case IV: temperatures inverted using ∂V_p and ∂V_s and Opx for its strengthening (red), weakening (green) and no (yellow) viscosity effects on Opx. This figure is available under CC-BY ?.

Nonetheless, we favor the differential stress calculations with the inverted temperatures and the presence of Opx (Case IV) because only they can explain the similar mag-

nitudes of the upper mantle Vp and Vs anomalies determined by Nyamwandha et al. (2016). The velocity anomalies cannot be attributed to elevated temperature alone, a more fertile mantle, or to the presence of fluids combined with elevated temperatures; the presence of elevated amounts of Opx is a necessary condition. The inverted values of Opx in the range of 5-45 % (Fig. 10) are similar to those found previously for the Kaapvaal Craton (Wagner et al., 2008) and the Colorado Plateau (Li, Lee, Peslier, Lenardic, & Mackwell, 2008). Metasomatism by Si rich fluids derived from a subducting slab is the preferred mechanism for Opx enrichment in these regions as documented by the texture and composition of mantle xenoliths (Bell et al., 2005; Li et al., 2008; Smith, Riter, & Mertzman, 1999).

The need for Opx enrichment to provide a reasonable explanation of the similar Vp and Vs anomalies argues for the presence of a slab below the Mississippi Embayment at some point in time. Flat subduction of the Farallon slab is usually invoked to explain deformation and magmatism during the Laramide orogeny (ca. 80 to 35 Ma) in the western U.S. (e.g., Humphreys, 2009) and several studies suggest that flat slab segments are present at depths above 1000 km in the central U.S. (Gao & Liu, 2014; Liu, Spasojevic, & Gurnis, 2008; Porritt, Allen, & Pollitz, 2014; Schmandt & Lin, 2014; Sigloch, 2011; Sigloch et al., 2008). Flattening of the Farallon slab can be attributed to the subduction of oceanic plateaus (the Shatsky and Hess plateaus) located on an old (>50 My) slab (e.g., English & Johnston, 2004; Liu et al., 2010). This situation would result in cold slab subduction, facilitating transport of hydrous minerals to transition zone depths (Kusky et al., 2014; Maruyama & Okamoto, 2007; Z. Wang, Kusky, & Capitanio, 2018). Geodynamic modeling by Liu et al. (2010) indicates that the top of the Hess plateau is located at a depth of about 660 km below the Mississippi Embayment (Figure 4 in (Liu et al., 2010)).

Seismic velocity models determined by tomographic inversion of teleseismic body waves also indicate the presence of high velocity regions at or below the transition zone in the central U.S. that are interpreted as fragments of the Farallon slab (e.g., Porritt et al., 2014; Schmandt & Lin, 2014; Sigloch, 2011; Sigloch et al., 2008). All of these models indicate the presence of a high velocity region in the vicinity of the Mississippi Embayment with, in general, shallower high velocities to the east of the NMSZ. The P and S wave velocity models determined by Porritt et al. (2014) indicate the presence of high velocities in the depth range 200 to 800 km below the Embayment and surrounding area.

In the depth range 400 to 600 km, the high velocity region is split by a band of low velocities that trends NNE, roughly along the western boundary of the Embayment. The low velocity band is either not present or cannot be resolved below 600 km. The low velocity band corresponds to the low velocity region imaged in the depth range 100 to 250 km below the Embayment in the higher resolution study by using TA and NELE FlexArray stations.

Biryol, Wagner, Fischer, and Hawman (2016) attribute the high velocity upper mantle region located to the east of the NMSZ to the presence of a dense, partially removed, lithospheric drip. The down-going drip may result in upward, return flow of the asthenosphere below the Reelfoot rift (Figure 9 in (Biryol et al., 2016)). Our analysis indicates that the V_p and V_s anomalies determined by Nyamwandha et al. (2016) cannot be attributed to the presence of asthenosphere devoid of Opx enrichment. One possibility that may be compatible with the concept put forth by Biryol et al. (2016) is that the upwelling asthenosphere was enriched in Opx by the presence of a slab fragment that has subsequently dropped to depths just below the transition zone. A deeper slab fragment is suggested by the tomography results of Schmandt and Lin (2014) and by the present location of the Hess oceanic plateau determined by Liu et al. (2010).

5 Conclusions

In this study, we explore possible explanations for the upper mantle V_p and V_s anomalies (∂V_p and ∂V_s), negative and of similar magnitudes, found below the Mississippi Embayment in the tomographic study by Nyamwandha et al. (2016) and suggest Opx enrichment as the most plausible one. When inverted for Opx volume fraction and temperature anomalies, these low velocity anomalies correspond to positive temperature anomalies up to 450 K and Opx contents of up to 40 %. The presence of Opx reduces the range of temperature variations, which is ± 600 K when converted from ∂V_p only. The estimated Opx fraction is in the range of estimates made for the Kaapvaal Craton (Wagner et al., 2008) and the Colorado Plateau (Li et al., 2008), which are associated with the water-rock interactions from the Chile–Argentina and Farallon flat slab, respectively. In NMSZ, olivine alteration to Opx might have been induced by fluids released from the flat-subducted Laramide slab.

We set up numerical viscoelastic models based on the tomography by Nyamwandha et al. (2016) to assess how variations in temperature, water and Opx contents affect the regional stress field in three dimensions. The concentration of stress from the weaker mantle into the stronger overlying crust has been indicated previously to explain the seismicity of the NMSZ (e.g., Kenner, 2000; Zhan et al., 2016). We observe similar stress-concentrating effects due to warm upper mantle indicated by the low velocity anomalies.

Acknowledgments

We thank C. Nyamwandha for access to the tomography data.

References

- Aagaard, B. T., Knepley, M. G., & Williams, C. A. (2013, jun). A domain decomposition approach to implementing fault slip in finite-element models of quasi-static and dynamic crustal deformation. *Journal of Geophysical Research: Solid Earth*, *118*(6), 3059–3079. Retrieved from <https://doi.org/10.1002/2Fjgrb.50217> doi: 10.1002/jgrb.50217
- Baird, A. F., McKinnon, S. D., & Godin, L. (2010, nov). Relationship between structures stress and seismicity in the Charlevoix seismic zone revealed by 3-D geomechanical models: Implications for the seismotectonics of continental interiors. *Journal of Geophysical Research*, *115*(B11). Retrieved from <https://doi.org/10.1029/2010jb007521> doi: 10.1029/2010jb007521
- Bakun, W. H., & Hopper, M. G. (2004, sep). Historical Seismic Activity in the Central United States. *Seismological Research Letters*, *75*(5), 564–574. Retrieved from <https://doi.org/10.1785/gssr1.75.5.564> doi: 10.1785/gssr1.75.5.564
- Bell, D. R., Grégoire, M., Grove, T. L., Chatterjee, N., Carlson, R. W., & Buseck, P. R. (2005, sep). Silica and volatile-element metasomatism of Archean mantle: a xenolith-scale example from the Kaapvaal Craton. *Contributions to Mineralogy and Petrology*, *150*(3), 251–267. Retrieved from <https://doi.org/10.1007/s00410-005-0673-8> doi: 10.1007/s00410-005-0673-8
- Biryol, C. B., Wagner, L. S., Fischer, K. M., & Hawman, R. B. (2016, may). Relationship between observed upper mantle structures and recent tectonic activity

- across the Southeastern United States. *Journal of Geophysical Research: Solid Earth*, *121*(5), 3393–3414. Retrieved from <https://doi.org/10.1002/2015jb012698> doi: 10.1002/2015jb012698
- Boyd, O. S., Smalley, R., & Zeng, Y. (2015, aug). Crustal deformation in the New Madrid seismic zone and the role of postseismic processes. *Journal of Geophysical Research: Solid Earth*, *120*(8), 5782–5803. Retrieved from <https://doi.org/10.1002/2015jb012049> doi: 10.1002/2015jb012049
- Burov, E. (2010, mar). The equivalent elastic thickness (T_e) seismicity and the long-term rheology of continental lithosphere: Time to burn-out “crème brûlée”? *Tectonophysics*, *484*(1-4), 4–26. Retrieved from <https://doi.org/10.1016/j.tecto.2009.06.013> doi: 10.1016/j.tecto.2009.06.013
- Calais, E., Han, J. Y., DeMets, C., & Nocquet, J. M. (2006, jun). Deformation of the North American plate interior from a decade of continuous GPS measurements. *Journal of Geophysical Research: Solid Earth*, *111*(B6), n/a–n/a. Retrieved from <https://doi.org/10.1029/2005jb004253> doi: 10.1029/2005jb004253
- Cammarano, F., Goes, S., Vacher, P., & Giardini, D. (2003, aug). Inferring upper-mantle temperatures from seismic velocities. *Physics of the Earth and Planetary Interiors*, *138*(3-4), 197–222. Retrieved from <https://doi.org/10.1016/s0031-9201%2803%2900156-0> doi: 10.1016/s0031-9201(03)00156-0
- Chen, C., Gilbert, H., Andronicos, C., Hamburger, M. W., Larson, T., Marshak, S., ... Yang, X. (2016, mar). Shear velocity structure beneath the central United States: implications for the origin of the Illinois Basin and intraplate seismicity. *Geochemistry Geophysics, Geosystems*, *17*(3), 1020–1041. Retrieved from <https://doi.org/10.1002/2015gc006206> doi: 10.1002/2015gc006206
- Chen, C., Zhao, D., & Wu, S. (2014, may). Crust and upper mantle structure of the New Madrid Seismic Zone: Insight into intraplate earthquakes. *Physics of the Earth and Planetary Interiors*, *230*, 1–14. Retrieved from <https://doi.org/10.1016/j.pepi.2014.01.016> doi: 10.1016/j.pepi.2014.01.016
- Chu, R., Leng, W., Helmberger, D. V., & Gurnis, M. (2013, sep). Hidden hotspot track beneath the eastern United States. *Nature Geoscience*, *6*(11), 963–966. Retrieved from <https://doi.org/10.1038/ngeo1949> doi: 10.1038/ngeo1949

- Cox, R., & Arsdale, R. V. (1997, jul). Hotspot origin of the Mississippi embayment and its possible impact on contemporary seismicity. *Engineering Geology*, 46(3-4), 201–216. Retrieved from [https://doi.org/10.1016/S0013-7952\(97\)00003-3](https://doi.org/10.1016/S0013-7952(97)00003-3) doi: 10.1016/S0013-7952(97)00003-3
- Cox, R. T., & Arsdale, R. B. V. (2002, sep). The Mississippi Embayment North America: a first order continental structure generated by the Cretaceous superplume mantle event. *Journal of Geodynamics*, 34(2), 163–176. Retrieved from [https://doi.org/10.1016/S0264-3707\(02\)00019-4](https://doi.org/10.1016/S0264-3707(02)00019-4) doi: 10.1016/S0264-3707(02)00019-4
- Dixon, J. E., Dixon, T., Bell, D., & Malservisi, R. (2004, may). Lateral variation in upper mantle viscosity: role of water. *Earth and Planetary Science Letters*, 222(2), 451–467. Retrieved from <https://doi.org/10.1016/j.epsl.2004.03.022> doi: 10.1016/j.epsl.2004.03.022
- English, J. M., & Johnston, S. T. (2004, sep). The Laramide Orogeny: What Were the Driving Forces? *International Geology Review*, 46(9), 833–838. Retrieved from <https://doi.org/10.2747/IGR.46.9.833> doi: 10.2747/IGR.46.9.833
- Gao, S. S., & Liu, K. H. (2014, aug). Mantle transition zone discontinuities beneath the contiguous United States. *Journal of Geophysical Research: Solid Earth*, 119(8), 6452–6468. Retrieved from <https://doi.org/10.1002/2014jb011253> doi: 10.1002/2014jb011253
- Goes, S., Govers, R., & Vacher, P. (2000, may). Shallow mantle temperatures under Europe from PandSwave tomography. *Journal of Geophysical Research: Solid Earth*, 105(B5), 11153–11169. Retrieved from <https://doi.org/10.1029/1999jb900300> doi: 10.1029/1999jb900300
- Goes, S., & van der Lee, S. (2002). Thermal structure of the north american uppermost mantle inferred from seismic tomography. *Journal of Geophysical Research: Solid Earth*, 107(B3), ETG–2.
- Grollmund, B., & Zoback, M. D. (2001). Did deglaciation trigger intraplate seismicity in the New Madrid seismic zone? *Geology*, 29(2), 175. Retrieved from [https://doi.org/10.1130/0091-7613\(2001\)029<0175:ddtisi>2.0.co;2](https://doi.org/10.1130/0091-7613(2001)029<0175:ddtisi>2.0.co;2) doi: 10.1130/0091-7613(2001)029<0175:ddtisi>2.0.co;2
- Hansen, L. N., & Warren, J. M. (2015, apr). Quantifying the effect of pyroxene on

- deformation of peridotite in a natural shear zone. *Journal of Geophysical Research: Solid Earth*, 120(4), 2717–2738. Retrieved from <https://doi.org/10.1002/2014jb011584> doi: 10.1002/2014jb011584
- Herzberg, C. T. (1983, may). Solidus and liquidus temperatures and mineralogies for anhydrous garnet-lherzolite to 15 GPa. *Physics of the Earth and Planetary Interiors*, 32(2), 193–202. Retrieved from [https://doi.org/10.1016/0031-9201\(83\)90139-5](https://doi.org/10.1016/0031-9201(83)90139-5) doi: 10.1016/0031-9201(83)90139-5
- Hirth, G., & Kohlstedt, D. (2003). Rheology of the upper mantle and the mantle wedge: A view from the experimentalists. In *Inside the subduction factory* (pp. 83–105). American Geophysical Union. Retrieved from <https://doi.org/10.1029/138gm06> doi: 10.1029/138gm06
- Humphreys, E. (2009, jun). Relation of flat subduction to magmatism and deformation in the western United States. *Geological Society of America Memoirs*, 204(0), 85–98. Retrieved from <https://doi.org/10.1130%2F2009.1204%2804%29> doi: 10.1130/2009.1204(04)
- Ji, S., Wang, Z., & Wirth, R. (2001, nov). Bulk flow strength of forsterite–enstatite composites as a function of forsterite content. *Tectonophysics*, 341(1-4), 69–93. Retrieved from [https://doi.org/10.1016/s0040-1951\(01\)00191-3](https://doi.org/10.1016/s0040-1951(01)00191-3) doi: 10.1016/s0040-1951(01)00191-3
- Johnston, A. C. (1996, aug). Seismic moment assessment of earthquakes in stable continental regions-III. New Madrid 1811-1812 Charleston 1886 and Lisbon 1755. *Geophysical Journal International*, 126(2), 314–344. Retrieved from <https://doi.org/10.1111/j.1365-246x.1996.tb05294.x> doi: 10.1111/j.1365-246x.1996.tb05294.x
- Karato, S. (2003). Mapping water content in the upper mantle. In *Inside the subduction factory* (pp. 135–152). American Geophysical Union. Retrieved from <https://doi.org/10.1029/138gm08> doi: 10.1029/138gm08
- Karato, S., & Jung, H. (1998, apr). Water partial melting and the origin of the seismic low velocity and high attenuation zone in the upper mantle. *Earth and Planetary Science Letters*, 157(3-4), 193–207. Retrieved from <https://doi.org/10.1016/s0012-821x%2898%2900034-x> doi: 10.1016/s0012-821x(98)00034-x
- Kenner, S. J. (2000, sep). A Mechanical Model for Intraplate Earthquakes: Ap-

- plication to the New Madrid Seismic Zone. *Science*, *289*(5488), 2329–2332. Retrieved from <https://doi.org/10.1126/science.289.5488.2329> doi: 10.1126/science.289.5488.2329
- Kennett, B. L. N., & Engdahl, E. R. (1991, may). Traveltimes for global earthquake location and phase identification. *Geophysical Journal International*, *105*(2), 429–465. Retrieved from <https://doi.org/10.1111/j.1365-246x.1991.tb06724.x> doi: 10.1111/j.1365-246x.1991.tb06724.x
- Kirby, S. H., & Kronenberg, A. K. (1987). Rheology of the lithosphere: Selected topics. *Reviews of Geophysics*, *25*(6), 1219. Retrieved from <https://doi.org/10.1029/rg025i006p01219> doi: 10.1029/rg025i006p01219
- Kusky, T. M., Windley, B. F., Wang, L., Wang, Z., Li, X., & Zhu, P. (2014, sep). Flat slab subduction trench suction, and craton destruction: Comparison of the North China, Wyoming, and Brazilian cratons. *Tectonophysics*, *630*, 208–221. Retrieved from <https://doi.org/10.1016%2Fj.tecto.2014.05.028> doi: 10.1016/j.tecto.2014.05.028
- Li, Z.-X. A., Lee, C.-T. A., Peslier, A. H., Lenardic, A., & Mackwell, S. J. (2008, sep). Water contents in mantle xenoliths from the Colorado Plateau and vicinity: Implications for the mantle rheology and hydration-induced thinning of continental lithosphere. *Journal of Geophysical Research*, *113*(B9). Retrieved from <https://doi.org/10.1029/2007jb005540> doi: 10.1029/2007jb005540
- Liu, L., Gurnis, M., Seton, M., Saleeby, J., Mller, R. D., & Jackson, J. M. (2010, mar). The role of oceanic plateau subduction in the Laramide orogeny. *Nature Geoscience*, *3*(5), 353–357. Retrieved from <https://doi.org/10.1038%2Fng829> doi: 10.1038/ng829
- Liu, L., Spasojevic, S., & Gurnis, M. (2008, nov). Reconstructing Farallon Plate Subduction Beneath North America Back to the Late Cretaceous. *Science*, *322*(5903), 934–938. Retrieved from <https://doi.org/10.1126/science.1162921> doi: 10.1126/science.1162921
- Liu, L., & Zoback, M. D. (1997, aug). Lithospheric strength and intraplate seismicity in the New Madrid seismic zone. *Tectonics*, *16*(4), 585–595. Retrieved from <https://doi.org/10.1029/97tc01467> doi: 10.1029/97tc01467
- Marshak, S., & Paulsen, T. (1996). Midcontinent U.S. fault and fold zones: A legacy of Proterozoic intracratonic extensional tectonism? *Geology*, *24*(2),

151. Retrieved from [https://doi.org/10.1130/0091-7613\(1996\)024<0151:musfaf>2.3.co;2](https://doi.org/10.1130/0091-7613(1996)024<0151:musfaf>2.3.co;2) doi: 10.1130/0091-7613(1996)024(0151:musfaf)2.3.co;2
- Maruyama, S., & Okamoto, K. (2007, jan). Water transportation from the subducting slab into the mantle transition zone. *Gondwana Research*, 11(1-2), 148–165. Retrieved from <https://doi.org/10.1016/j.gr.2006.06.001> doi: 10.1016/j.gr.2006.06.001
- McDonnell, R. D., Peach, C. J., van Roermund, H. L. M., & Spiers, C. J. (2000, jun). Effect of varying enstatite content on the deformation behavior of fine-grained synthetic peridotite under wet conditions. *Journal of Geophysical Research: Solid Earth*, 105(B6), 13535–13553. Retrieved from <https://doi.org/10.1029/1999jb900412> doi: 10.1029/1999jb900412
- Mooney, W., Andrews, M., Ginzburg, A., Peters, D., & Hamilton, R. (1983). Crustal Structure of the Northern Mississippi Embayment and a Comparison with other Continental Rift Zones. In *Processes of continental rifting* (pp. 327–348). Elsevier. Retrieved from <https://doi.org/10.1016/b978-0-444-42198-2.50025-0> doi: 10.1016/b978-0-444-42198-2.50025-0
- Nyamwandha, C. A., Powell, C. A., & Langston, C. A. (2016, may). A joint local and teleseismic tomography study of the Mississippi Embayment and New Madrid Seismic Zone. *Journal of Geophysical Research: Solid Earth*, 121(5), 3570–3585. Retrieved from <https://doi.org/10.1002/2015jb012761> doi: 10.1002/2015jb012761
- Pollitz, F. F. (2001, dec). Sinking Mafic Body in a Reactivated Lower Crust: A Mechanism for Stress Concentration at the New Madrid Seismic Zone. *Bulletin of the Seismological Society of America*, 91(6), 1882–1897. Retrieved from <https://doi.org/10.1785/0120000277> doi: 10.1785/0120000277
- Pollitz, F. F., & Mooney, W. D. (2014, sep). Seismic structure of the Central US crust and shallow upper mantle: Uniqueness of the Reelfoot Rift. *Earth and Planetary Science Letters*, 402, 157–166. Retrieved from <https://doi.org/10.1016/j.epsl.2013.05.042> doi: 10.1016/j.epsl.2013.05.042
- Porritt, R. W., Allen, R. M., & Pollitz, F. F. (2014, sep). Seismic imaging east of the Rocky Mountains with USArray. *Earth and Planetary Science Letters*, 402, 16–25. Retrieved from <https://doi.org/10.1016/j.epsl.2013.10.034> doi: 10.1016/j.epsl.2013.10.034

- Pujol, J., Johnston, A., Chiu, J.-M., & Yang, Y.-T. (1997, jul). Refinement of thrust faulting models for the Central New Madrid seismic zone. *Engineering Geology*, *46*(3-4), 281–298. Retrieved from <https://doi.org/10.1016%2Fs0013-7952%2897%2900007-0> doi: 10.1016/s0013-7952(97)00007-0
- Rabak, I., Langston, C., & Powell, C. (2011, jan). The Reelfoot Magnetic Anomaly and Its Relationship to the Pascola Arch and the Reelfoot Fault. *Seismological Research Letters*, *82*(1), 132–140. Retrieved from <https://doi.org/10.1785/gssrl.82.1.132> doi: 10.1785/gssrl.82.1.132
- Santosh, M., Zhao, D., & Kusky, T. (2010, jan). Mantle dynamics of the Paleoproterozoic North China Craton: A perspective based on seismic tomography. *Journal of Geodynamics*, *49*(1), 39–53. Retrieved from <https://doi.org/10.1016/j.jog.2009.09.043> doi: 10.1016/j.jog.2009.09.043
- Schmandt, B., & Lin, F.-C. (2014, sep). P and S wave tomography of the mantle beneath the United States. *Geophysical Research Letters*, *41*(18), 6342–6349. Retrieved from <https://doi.org/10.1002/2014gl061231> doi: 10.1002/2014gl061231
- Schutt, D. L., & Lesher, C. E. (2010, dec). Compositional trends among Kaapvaal Craton garnet peridotite xenoliths and their effects on seismic velocity and density. *Earth and Planetary Science Letters*, *300*(3-4), 367–373. Retrieved from <https://doi.org/10.1016/j.epsl.2010.10.018> doi: 10.1016/j.epsl.2010.10.018
- Sigloch, K. (2011, feb). Mantle provinces under North America from multifrequency Pwave tomography. *Geochemistry Geophysics, Geosystems*, *12*(2), n/a–n/a. Retrieved from <https://doi.org/10.1029%2F2010gc003421> doi: 10.1029/2010gc003421
- Sigloch, K., McQuarrie, N., & Nolet, G. (2008, jun). Two-stage subduction history under North America inferred from multiple-frequency tomography. *Nature Geoscience*, *1*(7), 458–462. Retrieved from <https://doi.org/10.1038/ngeo231> doi: 10.1038/ngeo231
- Smith, D., Riter, J. A., & Mertzman, S. A. (1999, jan). Water–rock interactions orthopyroxene growth, and Si-enrichment in the mantle: evidence in xenoliths from the Colorado Plateau, southwestern United States. *Earth and Planetary Science Letters*, *165*(1), 45–54. Retrieved from <https://doi.org/10.1016/>

- s0012-821x(98)00251-9 doi: 10.1016/s0012-821x(98)00251-9
- Sobolev, S. V., Zeyen, H., Stoll, G., Werling, F., Altherr, R., & Fuchs, K. (1996, mar). Upper mantle temperatures from teleseismic tomography of French Massif Central including effects of composition mineral reactions, anharmonicity, anelasticity and partial melt. *Earth and Planetary Science Letters*, 139(1-2), 147–163. Retrieved from [https://doi.org/10.1016/0012-821x\(95\)00238-8](https://doi.org/10.1016/0012-821x(95)00238-8) doi: 10.1016/0012-821x(95)00238-8
- Sundberg, M., & Cooper, R. F. (2008, dec). Crystallographic preferred orientation produced by diffusional creep of harzburgite: Effects of chemical interactions among phases during plastic flow. *Journal of Geophysical Research*, 113(B12). Retrieved from <https://doi.org/10.1029/2008jb005618> doi: 10.1029/2008jb005618
- Tang, Y.-J., Zhang, H.-F., Deloule, E., Su, B.-X., Ying, J.-F., Xiao, Y., & Hu, Y. (2012, sep). Slab-derived lithium isotopic signatures in mantle xenoliths from northeastern North China Craton. *Lithos*, 149, 79–90. Retrieved from <https://doi.org/10.1016/j.lithos.2011.12.001> doi: 10.1016/j.lithos.2011.12.001
- Tasaka, M., Hiraga, T., & Zimmerman, M. E. (2013, aug). Influence of mineral fraction on the rheological properties of forsterite+enstatite during grain-size-sensitive creep: 2. Deformation experiments. *Journal of Geophysical Research: Solid Earth*, 118(8), 3991–4012. Retrieved from <https://doi.org/10.1002/jgrb.50284> doi: 10.1002/jgrb.50284
- Tikoff, B., Larson, C. E., Newman, J., & Little, T. (2010, dec). Field-based constraints on finite strain and rheology of the lithospheric mantle Twin Sisters, Washington. *Lithosphere*, 2(6), 418–422. Retrieved from <https://doi.org/10.1130/197.1> doi: 10.1130/197.1
- Tuttle, M. P. (2002, aug). The Earthquake Potential of the New Madrid Seismic Zone. *Bulletin of the Seismological Society of America*, 92(6), 2080–2089. Retrieved from <https://doi.org/10.1785/0120010227> doi: 10.1785/0120010227
- Wagner, L. S., Anderson, M. L., Jackson, J. M., Beck, S. L., & Zandt, G. (2008). Seismic evidence for orthopyroxene enrichment in the continental lithosphere. *Geology*, 36(12), 935. Retrieved from <https://doi.org/10.1130/g25108a.1>

doi: 10.1130/g25108a.1

- Wang, Q., Bagdassarov, N., Xia, Q.-K., & Zhu, B. (2014, feb). Water contents and electrical conductivity of peridotite xenoliths from the North China Craton: Implications for water distribution in the upper mantle. *Lithos*, *189*, 105–126. Retrieved from <https://doi.org/10.1016/j.lithos.2013.08.005> doi: 10.1016/j.lithos.2013.08.005
- Wang, Z., Kusky, T. M., & Capitanio, F. A. (2018, jan). Water transportation ability of flat-lying slabs in the mantle transition zone and implications for craton destruction. *Tectonophysics*, *723*, 95–106. Retrieved from <https://doi.org/10.1016/j.tecto.2017.11.041> doi: 10.1016/j.tecto.2017.11.041
- Zhan, Y., Hou, G., Kusky, T., & Gregg, P. M. (2016, mar). Stress development in heterogeneous lithosphere: Insights into earthquake processes in the New Madrid Seismic Zone. *Tectonophysics*, *671*, 56–62. Retrieved from <https://doi.org/10.1016/j.tecto.2016.01.016> doi: 10.1016/j.tecto.2016.01.016
- Zhang, J.-J., Zheng, Y.-F., & Zhao, Z.-F. (2009, jun). Geochemical evidence for interaction between oceanic crust and lithospheric mantle in the origin of Cenozoic continental basalts in east-central China. *Lithos*, *110*(1-4), 305–326. Retrieved from <https://doi.org/10.1016/j.lithos.2009.01.006> doi: 10.1016/j.lithos.2009.01.006
- Zoback, M. D., Apel, R., Baumgärtner, J., Brudy, M., Emmermann, R., Engeser, B., ... Vernik, L. (1993, oct). Upper-crustal strength inferred from stress measurements to 6 km depth in the KTB. *Nature*, *365*(6447), 633–635. Retrieved from <https://doi.org/10.1038/365633a0> doi: 10.1038/365633a0
- Zoback, M. L., & Zoback, M. D. (1989). Chapter 24: Tectonic stress field of the continental United States. In *Geological society of america memoirs* (pp. 523–540). Geological Society of America. Retrieved from <https://doi.org/10.1130/mem172-p523> doi: 10.1130/mem172-p523